Supplementary Information: Photovoltaics-driven power production can support human exploration on Mars

Anthony J. Abel[a,b,†], **Aaron J. Berliner**[a,c,†], **Mia Mirkovic**[a,d], **William D. Collins**[e,f,*], **Adam P. Arkin**[a,b,g,*], **Douglas S. Clark**[a,c,h,*]

[†] These These authors contributed equally, [a] Center for the Utilization of Biological Engineering in Space (CUBES), Berkeley, CA 94720, USA, [b] Department of Chemical and Biomolecular Engineering, University of California, Berkeley, CA 94720, USA, [c] Department of Bioengineering, University of California, Berkeley, CA 94720, USA, [d] Department of Electrical Engineering and Computer Sciences, University of California, Berkeley, CA 94720, USA, [e] Climate and Ecosystems Sciences Division, Lawrence Berkeley National Laboratory, Berkeley, CA 94720, USA, [f] Department of Earth and Planetary Sciences, University of California, Berkeley, CA 94720, USA, [g] Environmental Genomics and Systems Biology Division, Lawrence Berkeley National Laboratory, Berkeley, CA 94720, USA, [h] Molecular Biophysics and Integrated Bioimaging Division, Lawrence Berkeley National Laboratory, Berkeley, CA 94720, USA

Correspondence*:
WDC, APA, or DSC.
wdcollins@lbl.gov,aparkin@lbl.gov,dsc@berkeley.edu

1 INTRODUCTION AND OVERVIEW

A central question surrounding possible settlement of Mars is whether human life can be supported by available technologies using *in situ* resources. Here we present a detailed analysis showing that photovoltaic and photoelectrochemical devices would be adequate and practical to sustain a crewed outpost for an extended period over a large fraction of the planet's surface. Climate data were integrated with a radiative transfer model to predict spectrally-resolved solar flux across the Martian surface, which informed detailed balance calculations for solar cell devices supporting power systems, agriculture, and manufacturing. Optimal design and the corresponding production capacity over a Martian year revealed the size and mass of a solar cell array required to support a six-person mission, which represents less than 10% of the anticipated payload.

The following SI describes the `redSun` software created as an integration of available software and custom code written in Python 3.6 with UNIX and Fortran backends. It can be found at https://github.com/cubes-space/redSun.

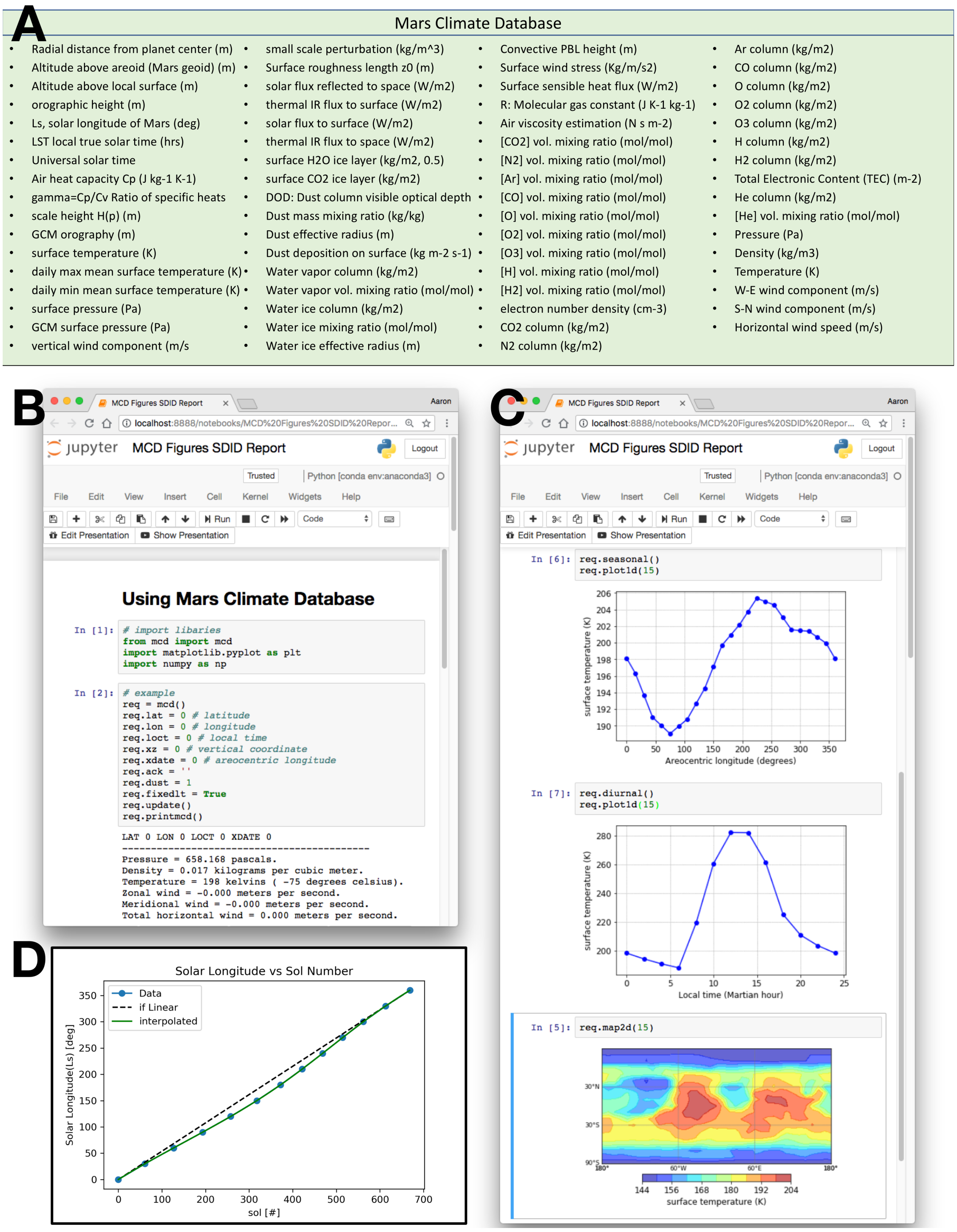

Figure 1. **(A)** all parameters available for query in the MCD; **(B.)** example query to MCD; **(C.)** i. plot of surface temperature vs areocentric longitude for local time t = 9:00; ii. plot of surface temperature vs local time for LATITUDE = LONGITUDE = 0; iii. cylindrical projection of surface temperature; **(D.)** Plot of solar longitude vs sol number, demonstrating the eccentricity of Mars's orbit and the approximate season, with northern summer solstice occurring when Ls = 90 and northern winter solstice when Ls = 270.

2 ENVIRONMENTAL DATA AGGREGATION

2.1 Mars Climate Database

Downstream radiative transfer calculations require a number of input streams describing the Martian environment. We make use of the Mars Climate Database (MCD) [1] developed by Le Laboratoire de

Meteorologie Dynamique (LMD) in Paris, queried via the mcd-python package, to model most climate and environmental constraints, including photon flux and power spectra over time and location. The software engineering processes for building and using MCD somewhat efficiently are illustrated in Figure 1, along with input parameter profiles and sample output plots.

2.2 Initial Geotemporalspatial Grid

We began by first initializing the geotemporalspatial grid from which all downstream radiative transfer and PV/PEC calculations would be based. The grid was composed as a `.netCDF` file with dimensions of 19 points of 10° latitude × 37 points of 10° longitude × 25 points of 15° areocentric longitude × 13 points of 2 (Martian) hours. Additionally, we included the dimension of altitude above the Martian datum in 20 points ranging from 0 to 120 km. The dimensions for the initial grid are shown in Table 1.

Dimension	Units	Initial	Final	Step	Number
Latitude	degrees north	-90	90	15	19
Longitude	degrees east	-180	180	15	37
Wavelength	nm	300.5	4000	N/A	1340
Level	km	0	120	6.32	20
Aerocentric Longitude	deg	0	360	15	25
Hour	hr	0	24	2	13

Table 1. Initial grid dimensions.

2.3 Atmospheric Variables

Through a combination of custom code in redSun and modifications to the Python-based extension of MCD, we then looped through Lat, Lon, Hr, and Ls dimensions to initialize the data variables in Table 2.

2.4 Planetary Variables

While most of the required environmental variables could be sourced from MCD, additional efforts were made to add data on the planetary albedo and zMOL as shown in Figure 2 and in Table 3.

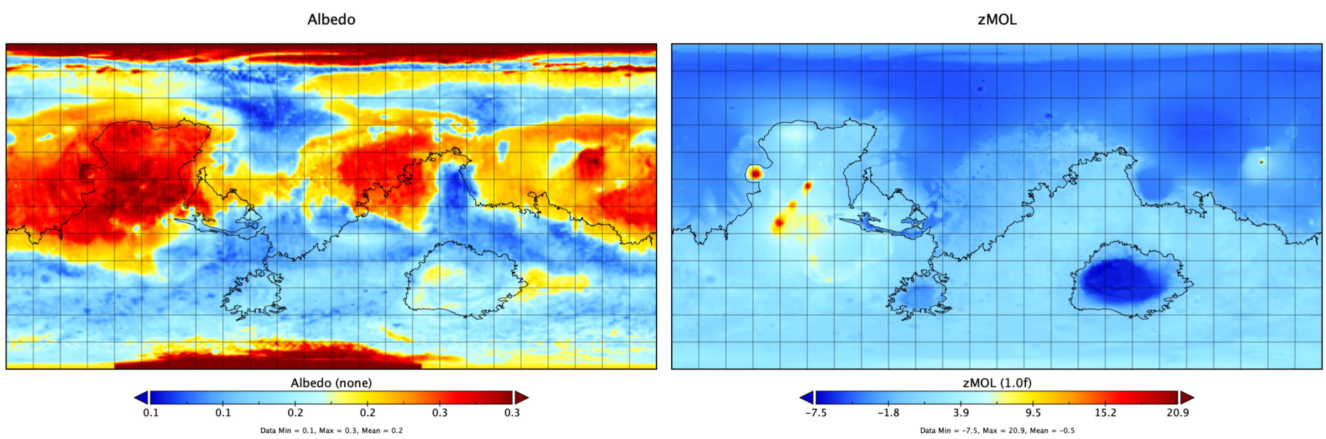

Figure 2. Albedo and zMOL (height above the Martian datum) maps.

Variable	Units	Dimensions	Dimension Number
Air Density	cm^{-3}	lat,lon,level,ls,hr	5
Datum Altitude	km	lat,lon,level	3
CO_2 Partial Pressure	cm^{-3}	lat,lon,level,ls,hr	5
H_2O Partial Pressure	cm^{-3}	lat,lon,level,ls,hr	5
O_2 Partial Pressure	cm^{-3}	lat,lon,level,ls,hr	5
O_3 Partial Pressure	cm^{-3}	lat,lon,level,ls,hr	5
NO_2 Partial Pressure	cm^{-3}	lat,lon,level,ls,hr	5
Pressure	hPa	lat,lon,level,ls,hr	5
Temperature	K	lat,lon,level,ls,hr	5
Ice Content	g/m^3	lat,lon,level,ls,hr	5
Ice Effective Radius	um	lat,lon,level,ls,hr	5
Dust Content	g/m^3	lat,lon,level,ls,hr	5
Dust Effective Radius	μm	lat,lon,level,ls,hr	5
Long Wave Downward Flux	W/m^2	lat,lon,ls,hr	4
Short Wave Downward Flux	W/m^2	lat,lon,ls,hr	4
Long Wave Upward Flux	W/m^2	lat,lon,ls,hr	4
Short Wave Upward Flux	W/m^2	lat,lon,ls,hr	4
Top of Atmosphere Irradiance	$W/(nm.m^2)$	lat,ls,hr,wl	5

Table 2. Initial atmospheric grid variables sourced from MCD.

i

Variable	Units	Dimensions	Dimension Number
Albedo	None	lat,lon	2
zMOL	None	lat,lon	2

Table 3. Initial planetary grid variables sourced from MCD.

2.5 Solar Variables

In addition to atmospheric and planetary variables, our initial environmental data for downstream radioactive transfer required that we calculate the solar flux at the top of the atmosphere (TOA). Downstream radiative transfer calculations required as input the spectral flux in $W/(m^2{\cdot}nm)$ whereas MCD only provided an integrated solar flux in $W/(m^2)$. For a given Lat, Lon, Hr, and Ls, we were able to calculate the spectral flux F_0 via[2]

$$F_0 = \mu F_{1.52}\left(\frac{d^2}{r^2}\right) \tag{1}$$

$$F_0 = F_{1.52}\left(\sin\theta\sin\epsilon\sin L_s + \cos\theta\cos\left(\frac{2\pi t}{P}\right)\left(1-\sin^2\epsilon\sin^2 L_s\right)^{1/2}\right)\left(\frac{1+e\cos(L_s-L_{s,p})}{1-e^2}\right)^2 \tag{2}$$

where r is the Sun-Mars distance along its orbit, d is the mean Sun-Mars distance of 1.52 AU, μ is the cosine of the solar zenith angle z, e is the Martian eccentricity ($e = 0.0934$), L_s is the aerocentric longitude, $L_{s,p}$ is the aerocentric longitude of perihelion (250°), θ is the latitude, ϵ is the Martian obliquity (25.2°), P is the duration of the Martian solar day (88775 s), t is any time measured from local noon, and $F_{1.52}$ is the flux at the average Sun-Mars distance[3].

While the separation of the aerocentric longitude and hourly time dimensions was helpful in indexing our grid, these two dimensions are related. For any aerocentric longitude index, there are 13 time points, and as these times correspond to movement of Mars around the sun, so does the aerocentric longitude. Therefore, when computing the TOA flux F_0, we updated L_s to correspond to the change in time t using the build in functions `Ls2Sol` and `Sol2Ls` from the `MCD` package. These functions relate L_s and t through Kepler's Problem via

$$L_s = \left(\nu \frac{180}{\pi} + L_{s,p}\right)(mod360) \tag{3}$$

$$\nu = 2\arctan\left[\sqrt{\frac{1+e}{1-e}}\tan\left(\frac{E}{2}\right)\right] \tag{4}$$

$$M = E - e\sin E = 2\pi\frac{D_s - t_p}{N_s} \tag{5}$$

where D_s is the sol number, t_{peri} is the time at perihelion, N_s is the number of sols in a Martian year, ν is the true anomaly, E is the eccentric anomaly, M is the mean anomaly, and N_s is the number of sols in a Martian year.

The data variables shown in Figure 3 were then added to the grid for downstream use as shown in Table 4.

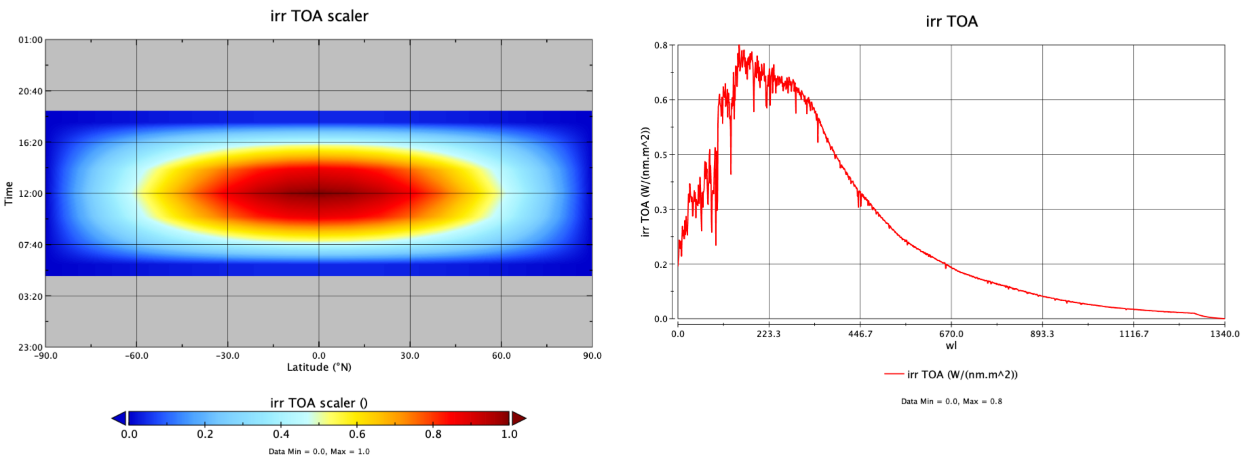

Figure 3. Left shows the calculated mu parameter as a scalar across geospace for $L_s = 0$. Right shows the spectral flux for lat=0, t=12 noon, and $L_s = 0$.

Variable	Units	Dimensions	Dimension Number
Solar Zenith Angle	deg	lat,ls,hr	3
Solar Correction	None	lat,ls,hr	3
Top of Atmosphere Irradiance	W/(nm.m^2)	lat,ls,hr,wl	5

Table 4. Initial solar grid variables.

As a sanity check, we calculated the integrated standard solar flux at TOA at 1.52 AU (average Sun-Mars distance) at 576.92 W/m^2. Given a solar constant for Mars is 490 W/m^2, the equatorial annual-mean flux at the top of the atmosphere (TOA) should be $\sim$156 W/m^2. Our calculated equatorial annual-mean TOA flux was found to be 159.43 W/m^2 which differs by $\sim$1.5% from the theoretical value. We extended this calculation across all latitudes as shown in Figure 4 to confirm our methods.

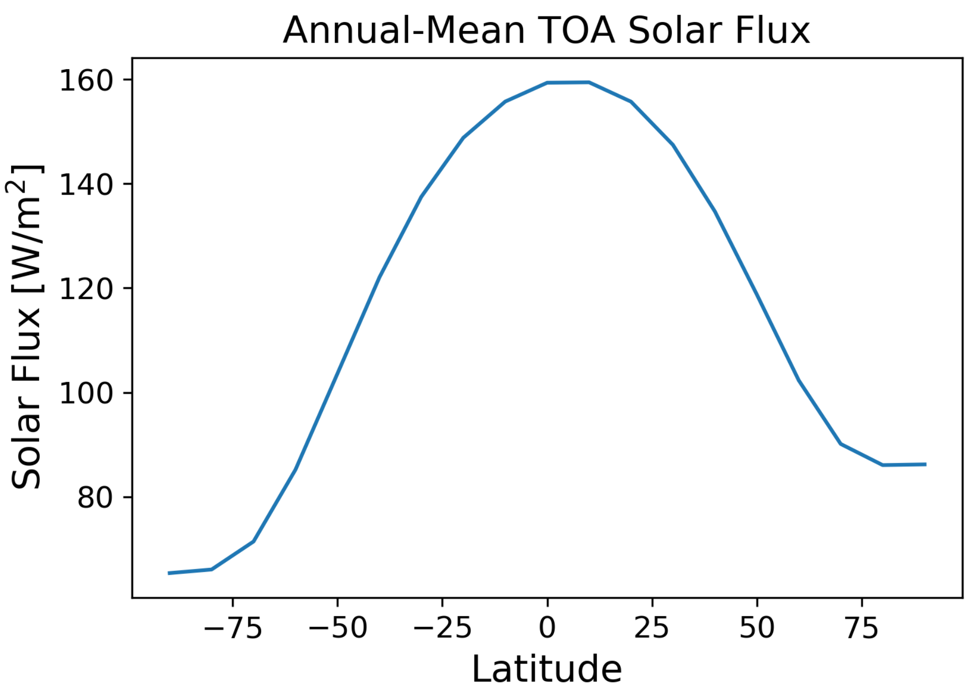

Figure 4. Calculated Annual-Mean TOA Solar Flux distributed across Latitude

3 RADIATIVE TRANSFER CALCULATIONS

3.1 libRadtran

The radiative transfer calculations were carried out using the libRadtran library (version 2.0.4)[4, 5]. libRadtran is a collection of C and Fortran functions and programs for calculation of solar and thermal radiation in the Earth's atmosphere and is freely available under the GNU General Public License at http://www.libradtran.org/doku.php.

3.2 Mie Scattering Calculations

The presence of dust and cloud particles in the Martian atmosphere affect the propagation of sunlight. The size of such dust and cloud particles falls within the Mie scattering range.

The libRadtran package was used for Mie scattering calculations of the scattering phase matrices and corresponding Legendre polynomials[6]. Input files for both dust and ice were constructed (Listing 1) and fed to the MIEV0 tool.

```
mie_program MIEV0 # Select Mie code by Wiscombe
basename cloud.
refrac file MieCloudRefrac.DAT# Use refractive index file
r_eff 0.00322766 100.1 10.0  # Specify effective radius grid
distribution lognormal 1.8903 # Specify lognormal size distribution
nstokes 1 # Calculate all phase matrix elements
nmom 6000 # Number of Legendre terms to be computed
```

```
nthetamax 2000 # Maximum number of scattering angles to be
output_user netcdf # Write output to netcdf file
verbose # Print verbose output
```

Listing 1. Input file for Mie calculations of cloud aerosols

Refractive indices for dust and ice were sourced from NASA Ames Legacy Mars Global Climate Model[7] (available at https://github.com/nasa/legacy-mars-global-climate-model) and fed as input (Figure 5).

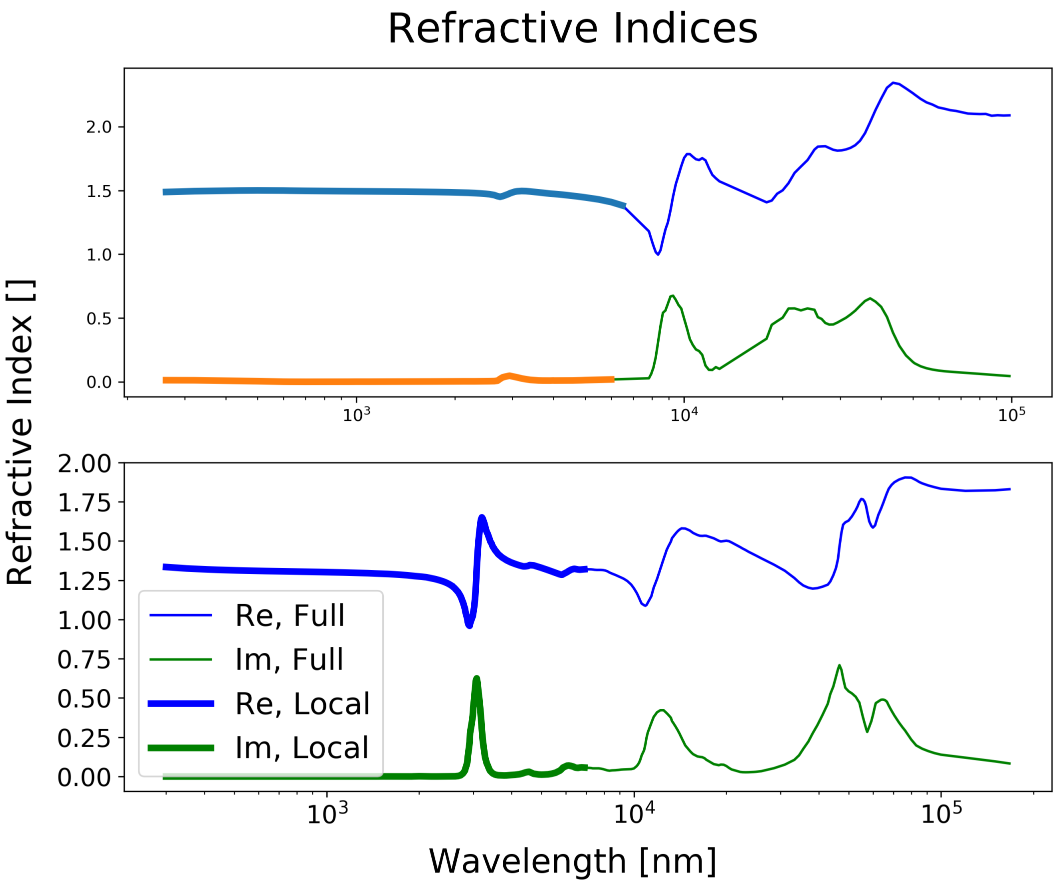

Figure 5. Refractive Indices for Dust (top) and Clouds (Bottom).

For clouds, an effective radius r_{eff} grid was set between 0.00322766 and 100.1 μm in steps of 10 μm and with a lognormal distribution with standard deviation $\sigma = 1.8903$ described as

$$n(r) = \frac{a}{r} \exp\left(-\frac{1}{2}\left(\frac{\ln(r)\ln(r_0)}{\ln \sigma}\right)^2\right) \tag{6}$$

where r_0 is the logarithmic mode of the distribution, calculated from r_{eff}. Through a series of trial-and-error attempts, we specified additional parameters for clouds such as the number of phase matrix elements set at 1, the number of Legendre terms to be computed set at 6000, the maximum number of scattering angles set to 2000. The resulting output from `MIEV0` was a `.netCDF` file of $\sim$100 MB.

For dust, an effective radius r_{eff} grid was set between 0.00310352 and 10.1 μm in steps of 1.0 μm and with a lognormal distribution with standard deviation $\sigma = 1.3616$. Again, through a series of trial-and-error attempts, we specified additional parameters for dust such as the number of phase matrix elements set at 1, the number of Legendre terms to be computed set at 2500, the maximum number of scattering angles set to 2000. The dust calculations provided more computationally expensive than those for clouds due to the smaller r_{eff} grid size. The resulting output from `MIEV0` was a `.netCDF` file of ~10 MB.

The output `.netCDF` files include the dimensions and variables in Table 5 and a sample of the output variables are shown in Figure 6.

Name	Description	Dim/Var	Unit
nlam	Wavelength Number	Dim	-
nmommax	Legendre Polynomial Number	Dim	-
nphamat	Phase Matrix Element Number	Dim	-
nreff	Refractive Index Number	Dim	-
nthetamax	Theta Max Number	Dim	-
nrho	Density Number	Dim	-
wavelen	Wavelength	Var	micrometer
reff	Effective radius	Var	micrometer
ntheta	Number of scattering angles	Var	-
theta	Theta Max Number	Var	degrees
phase	phase	Var	-
nmom	number of Legendre polynomials	Var	-
pmom	Legendre polynomials	Var	including factor 2*l+1
ext	extinction coefficient	Var	km^-1/(g/m^3)
ssa	single scattering albedo	Var	-
gg	Asymmetry factor	Var	-
refre	refractive index (real)	Var	-
refim	refractive index (imaginary)	Var	-
rho	density of medium	Var	g/cm^3

Table 5. Dimensions and variables in `.netCDF` Mie output file.

3.3 uvspec

The `uvspec` program was designed to calculate the radiation field of the atmosphere for Earth. Modifications were carried out such that `uvspec` could be leveraged for similar calculations of the Martian radiative transfer. Input to the model are the constituents of the atmosphere including various molecules, aerosols and clouds. The absorption and scattering properties of these constituents were calculated via the `MIEV0` tool. Boundary conditions are the solar spectrum at the top of the atmosphere and the reflecting surface at the bottom[8]. The `uvspec` program was called for each point in the geotemporalspatial grid and provided with a custom, programmatically generated input file – an example of which is shown in Listing 2.

```
# libRadtran Calc test
wavelength 300.5 4000 # choose wavelength range for computation
atmosphere_file __2WKSII17KGatmos.DAT # load atmosphere profile
mixing_ratio CH4 0.0 # update null mixing ratios
mixing_ratio N2O 0.0
mixing_ratio F11 0.0
mixing_ratio F12 0.0
mixing_ratio F22 0.0
altitude -0.48425 # specify altitude above datum
```

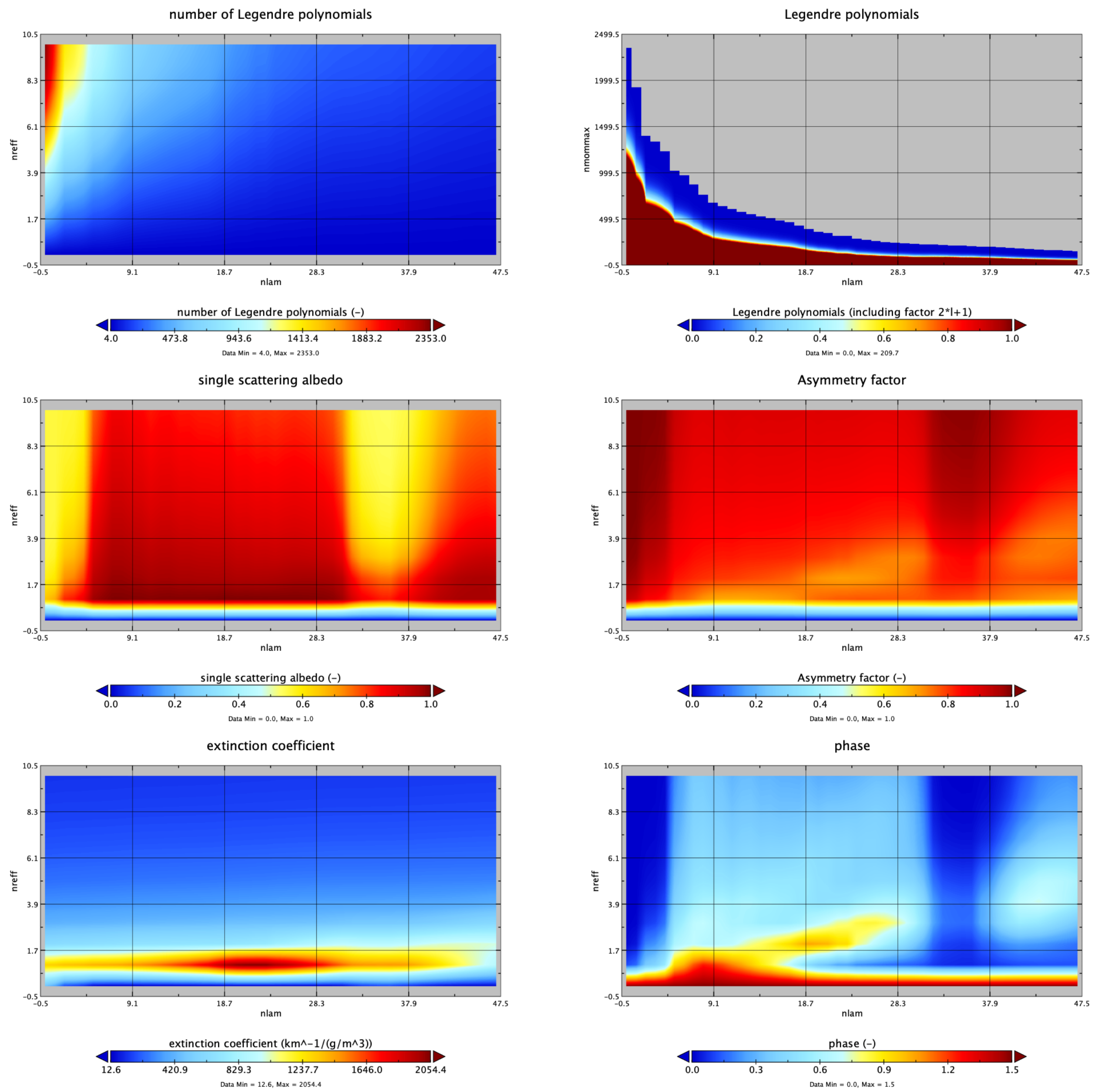

Figure 6. Sample Visualization of variables in `.netCDF` Mie output file for dust.

```
source solar __2WKSII17KGflux.DAT # load solar profile
# corrected for Sun-Mars Distance
# corrected for geometry
ic_file 1D __2WKSII17KGcloud.DAT # setup cloud profile (assuming water/ice clouds)
ic_properties MieCalc/cloud.mie.cdf interpolate
profile_file dust 1D __2WKSII17KGdust.DAT # setup dust profile (using aerosol type)
profile_properties dust MieCalc/dust.mie.cdf interpolate
earth_radius 3389.5 # reset earth_radius to Martian radius in [km]
rte_solver disort pseudospherical # choose radiative transfer solver
pseudospherical
number_of_streams 6 # choose number of streams
output_user lambda edir eglo edn eup enet esum # define output
```

```
albedo 0.3073502629995346 # choose albedo
```

Listing 2. Sample input file for uvspec calculation

Due to the peculiar way `uvspec` must be called, input for atmosphere, solar flux, dust conditions, and cloud conditions are required in the form of text-based `.DAT` files. Because multiple `uvspec` calls were carried out in parallel, a random string was generated ("2WKSII17KG" in the case of Listing 2) and used to identify specific `.DAT` files. For each point of the grid, an input `.INP` file was created along with correspond `.DAT` files for atmosphere, solar flux, dust conditions, and cloud conditions. The atmosphere file contained the altitude above sea level in km, pressure in hPa, temperature in K, air density in cm^{-3}, ozone density in cm^{-3}, Oxygen density in cm^{-3}, water vapor density in cm^{-3}, CO_2 density in cm^{-3}, and NO_2 density in cm^{-3}. The dust and cloud aerosol files contained altitude above sea level in km, dust/cloud content in kg/kg, and effective radius in μm. The solar flux file contains the wavelength in nm and the spectral flux for that wavelength in mW/(m^2nm). Data for each of these files was sourced from the MCD data organized in the `Stupidgrid.nc` file and converted to the appropriate units using functions in the `redSun` codebase.

The wavelength range was set from 300.5 to 4000 nm. This range was selected to match available data for solar flux and significance to downstream photovoltaic calculations. Wavelengths outside these bounds were found to have negligible impact on bandgap calculations or to require substantial computational efforts, and were thus ignored. The mixing ratios for atmospheric CH_4, N_2O, and greenhouse gases (GHG) F11, F12, and F22 were set to 0.0 to reflect the change from Earth to Mars conditions. The altitude for the location was also programmatically added to the input file to specify the exact position of the surface in relationship to the Martian datum. The filenames from the Mie scattering calculations for dust and cloud aerosols were passed as well. The radius of the planet was changed to the Martian value of 3389.5 km. The albedo of the grid-point was also provided programmatically.

We selected the DIScrete ORdinate Radiative Transfer solvers (`pseudospherical disort`) radiative transfer solver for our calculations using 6 streams. The discrete ordinate method was first developed in 1960 with significant updates in 1988 and 2000 and offer 1D calculations of radiance, irradiance, and actinic flux. We opted for pseudo-spherical methods to offset any spherical effects associated with using the smaller Martian geometry. In pseudo-spherical calculations, the monochromatic radiative transfer equation in 1D can be formulated as

$$\mu \frac{dI(\tau,\mu,\phi)}{\beta^{\text{ext}} d\tau} = I(\tau,\mu,\phi) - \frac{\omega(r)}{4\pi}\int_0^{2\pi} d\phi' \int_{-1}^{1} d\mu' p(\tau,\mu,\phi;\mu',\phi') I(\tau,\mu',\phi') - (1-\omega(r))B[T(r)] - \frac{\omega(\tau) I^0}{4\pi} p(\tau, \tag{7}$$

where $B[T(r)]$ is the Planck function, β is an extinction coefficient, μ_0 is the solar zenith angle, ϕ_0 is the azimuth angle, p is the phase function, and the single scattering albedo $\omega(r)$ is

$$\omega(r) = \omega(r,\nu) = \frac{\beta^{\text{sca}}(r,\nu)}{\beta^{\text{ext}}(r,\nu)} \tag{8}$$

Additionally, f_{ch} is the Chapman function[9, 10] for describing the extinction path in a spherical atmosphere and is formulated as

$$f_{ch}(r_0,\mu_0) = \int_{r_0}^{\infty} \frac{\beta^{\text{ext}}(r,\nu)dr}{\sqrt{1-\left(\frac{R+r_0}{R+r}\right)^2(1-\mu_0^2)}} \tag{9}$$

where R is the planet radius and r_0 is the distance above the atmosphere.

The output of each `uvspec` call was a text-like file that was indexed with a matching random string identifier. Each file consisted of the direct, global, diffuse downward, diffuse upward, net and sum irradiance in mW/(m^2nm) for each nm in the input flux file. The output file was then read back with additional functions from `redSun` for use in downstream calculations.

4 PHOTOVOLTAIC POWER AND PHOTOELECTROCHEMICAL COMMODITY CALCULATIONS

We use the detailed balance model to calculate the energy efficiency of one-, two-, and three-bandgap photovoltaic solar cells and one- and two-bandgap photoelectrochemical devices. This model has been used to calculate the limiting efficiency of ideal photovoltaic and photoelectrochemical devices for single and multiple bandgap architectures previously[11, 12, 13].

The current density (J)-voltage (V) dependence $J\,(V, E_g)$ for a single bandgap is given by

$$J\,(V, E_g) = J_G(E_g) + J_R(V, E_g) \tag{10}$$

where J_G is the photogeneration current, J_R is the recombination current due to radiative recombination, and E_g is the bandgap of the absorber material. The generation current J_G is calculated according to

$$J_G(E_g) = q \int_{E_g}^{E_{\text{max}}} \Gamma(E) dE \tag{11}$$

where q is the electronic charge, $\Gamma(E)$ is the photon flux at a given photon energy E, and E_{max} is maximum photon energy in the solar spectrum. We used a minimum wavelength of 300 nm in our calculations, corresponding to a maximum photon energy of $\sim$4.14 eV because photons above 4 eV contribute negligibly to the photon flux[11]. The recombination current density J_R is calculated according to

$$J_R(V, E_g) = \frac{2\pi q}{c^2 h^3} \int_{E_g}^{\infty} \frac{E^2}{\exp\left(\frac{E - qV}{kT}\right) - 1} dE \tag{12}$$

where c is the speed of light in vacuum, h is Planck's constant, k is Boltzmann's constant, and T is the temperature of the device (we assume the local surface temperature in these calculations).

The photovoltaic energy efficiency η_{PV} at a given operating voltage is written as

$$\eta_{\text{PV}}(V, E_g) = \frac{V}{F} J(V, E_g) \tag{13}$$

where F is the calculated total power flux at the Martian surface. The operating voltage can then be selected to maximize the efficiency for a given bandgap. In technoeconomic calculations (see below), we assume the device efficiency is 80% of the calculated detailed balance limit to account for absorber material and device inefficiencies (i.e., nonradiative recombination losses not captured by the detailed balance limit).

The photoelectrochemical device energy efficiency η_{PEC} is given by

$$\eta_{\text{PEC}}(V, E_g) = \frac{E^0}{F} J(V, E_g) \tag{14}$$

where E^0 is the minimum thermodynamic potential required to drive the electrochemical reaction (1.23 V for H_2 generation from water splitting). In practical devices, the operating voltage of the photoelectrochemical device will be larger than E^0 to account for anode and cathode overpotentials and resistive potential drop in the electrolyte and electrodes. Hence, for these devices the operating voltage is

$$V = E^0 + V_o \tag{15}$$

where V_o is the overpotential associated with the above-mentioned losses. In all technoeconomic calculations (see below) we assume the overvoltage is 700 mV, corresponding to a practical minimum that also accounts for absorber material inefficiencies (*i.e.*, nonradiative recombination losses not captured by the detailed balance limit)[12].

For two- and three-bandgap tandem devices, we assume the absorber layers are connected optically and electronically in series. Generation and recombination currents are calculated as described above, with the modification that E_{max} is substituted with $E_{g,n-1}$ for absorber n (counted sequentially starting with the top absorber) to reflect the assumption that each absorber layer is optically thick (i.e, absorbs all the above-bandgap light incident on its surface). In tandem devices, the total current density must be equal in each absorber layer, while the total operating voltage is given by the sum of the voltages developed across each cell. For example, for a three-absorber photovoltaic device

$$J(V) = J_1(V_1, E_{g,1}) = J_2(V_2, E_{g,2}) = J_3(V_3, E_{g,3}) \tag{16}$$

$$V = V_1 + V_2 + V_3 \tag{17}$$

For tandem devices, the efficiency is calculated analogously to the single-junction devices but as a function of each absorber bandgap.

5 GRID CALCULATIONS VIA PARALLEL COMPUTING

5.1 SinglePoint Calculation

The calculation of a single gridpoint's spectral flux (via `libRadtran`) and the corresponding photovoltaic and photoelectrochemical production quantities ran for $\sim$5 minutes. Given the grid of 228475 geotemporalspatial points composed of 19 points of 10° latitude × 37 points of 10° longitude × 25 points of 15° areocentric longitude × 13 points of 2 (Martian) hours, a serial calculation would require 2.17 years. Wanting to avoid that lengthy calculation, we opted for an "embarrassingly parallel" computing method shown in Figure 7. Since our computations require some initial or final communication (generally in the distribution and collection of data, then we call it nearly embarrassingly parallel. In parallel computing, an embarrassingly parallel workload or problem is one where little or no effort is needed to separate the problem into a number of parallel tasks. This is often the case where there is little or no dependency or need for communication between those parallel tasks, or for results between them. In the ideal case, all the sub-problems or tasks are defined before the computations begin and all the sub-solutions are stored in

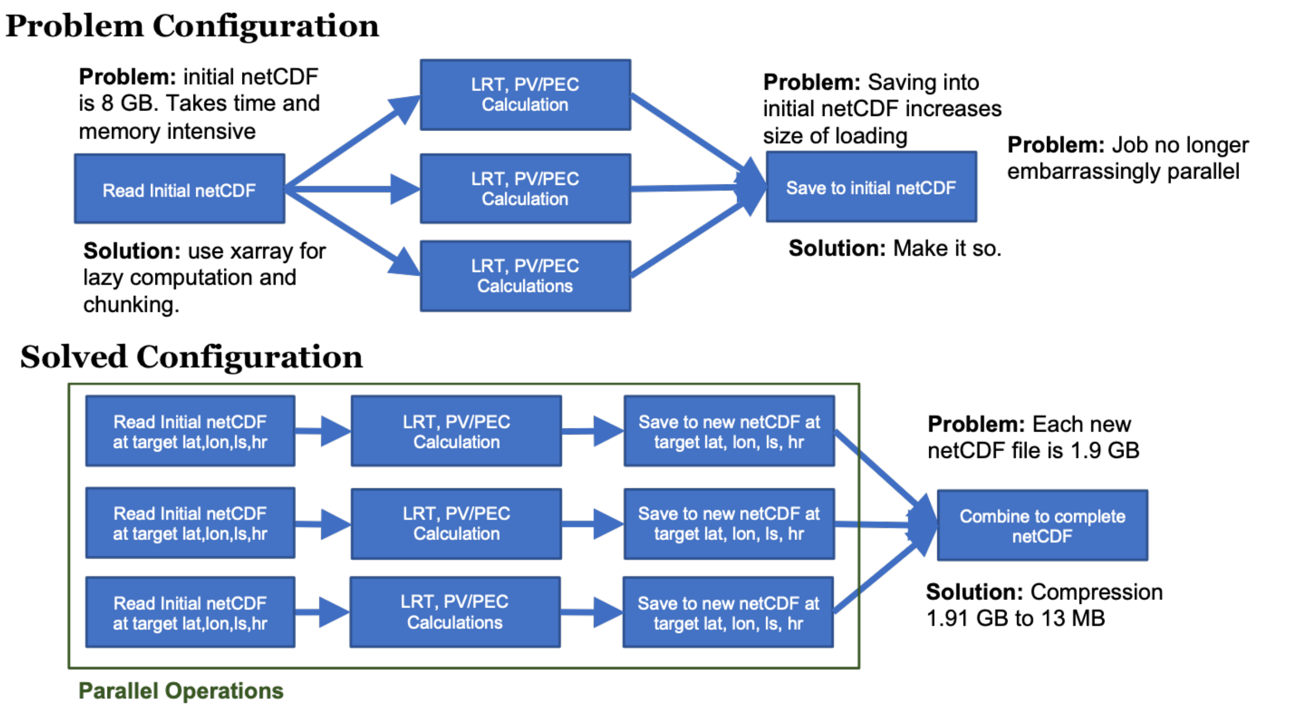

Figure 7. Initial (problem) and final (solution) configurations for the RedSun software on the UC Berkeley cluster.

independent memory locations (variables, array elements). Thus, the computation of the sub-solutions is completely independent[1].

Files were not constructed for grid-points that did not receive sunlight, and so the result was the storage of ∼150k `.netCDF` files, each with a size of ∼4-5 MB.

5.2 Stitching

The ∼150k singlepoint `.netCDF` files were initially stitched across time dimensions of hours and areocentric longitude to produce ∼700 time series `.netCDF` files, each for a different pair of latitudes and longitudes using the `tcsh` scripts provided in Listing 3 and 4.

```
#!/bin/tcsh -f
if ($#argv != 1) then
   echo "--> usage: csh " $0 " netcdf_file"
   exit
endif
set link = `ncdump -v ls,hr,lat,lon $argv[1] | sed -n '/^data:/,$p' | sort | paste -s -d" " - | awk '{
    printf("%s%03d%02d%s%02d%s%02d%s\n","ttlrecall_",$15,$3,"_",$11,"_",$7,".nc");}'`
ln -sv $argv[1] $link
```

Listing 3. Stitching Algorithm Part 1: Create Dynamic Links

```
#!/bin/tcsh -f
set lat = minimum_lat_value
set lon = minimum_lon_value
while ($lat <= maximum_lat_value)
```

[1] https://www.cs.iusb.edu/~danav/teach/b424/b424_23_embpar.html

```
    set latv = `echo $lat | awk '{printf("%02d\n",$1)}'`
    while ($lon <= maximum_lon_value)
            set lonv = `echo $lon | awk '{printf("%02d\n",$1)}'`
            ncecat ttlrecall_*_{$lonv}_{$latv}.nc redsun_timeseries_{$lonv}_{$latv}.nc
            echo "Done: " $lonv $latv
@ lon++
     end
@ lat++
end
```

Listing 4. Stitching Algorithm Part 2: Assemble into Time Series

5.3 Production Mapping

The resultant timeseries `.netCDF` files were then used for constructing the final maps of PV and PEC production. For each time series `.netCDF` file, we began by calculating PV power P and PEC production rate $\dot{m}$ via

$$P = \Gamma\eta_{\text{pv}} \tag{18}$$

$$\dot{m}_c = \epsilon_c \Gamma \eta_{\text{pec}} = \frac{Z_c}{n_c V_c F}\Gamma\eta_{\text{pec}} \tag{19}$$

where Γ is the solar flux in W/m^2 sourced from the `MCD` data in `StupidGrid.nc`, ϵ is the electrochemical equivalency factor, η is the calculated PV/PEC efficiency, Z is the molar mass, n is the number of moles of electrons required to make one mole of the product, F is the Faraday constant, and V is the voltage. The c term corresponds to the chemical of interest in the set of H_2, NH_3, and AA. The values used to produce the ϵ for each chemical is given in Table 6.

Chemical	n	Z	V
H_2	2	2.016	1.23
NH_3	6	17.031	1.17
AA	8	60.052	1.09

Table 6. Electrochemical equivalency factor parameters.

We calculated the optimal sol-averaged 3-junction PV P_{opt} and 2-junction PEC $\dot{m}_{\text{copt}}$ across all bandgap combinations given the form

$$P_{\text{opt}} = \max\left(\frac{1}{N}\int_{t_2}\int_{t_1} P_{ijk}\,dt_1 dt_2 : \forall i,j,k \in B_1, B_2, B_3\right) \tag{20}$$

$$\dot{m}_{c,opt} = \max\left(\frac{1}{N}\int_{t_2}\int_{t_1} \dot{m}_{c,ij}\,dt_1 dt_2 : \forall i,j \in B_1, B_2\right) \tag{21}$$

where i, j, k are indices of bandgaps B_1, B_2, B_3, t_1 is the time variable across a sol (~24.616 hrs/sol), and t_2 is the time variable across a Martian year given as $N = 688$ sols/year.

Computationally, we began by converting our L_s values to the sol number using an inverted Kepler problem with a function `ls2sol` shown in Listing 5.

```
def ls2sol(ls):
```

```
    N_s = 668.6
    ls_peri = 250.99
    t_peri = 485.35
    a = 1.52368
    e = 0.09340
    epsilon = 25.1919
    if (ls == 0).any():
        ls = .01
    nu = np.radians(ls) + 1.90258
    E = np.arctan((np.tan(nu/2))/(np.sqrt((1+e)/(1-e))))*2
    M = E - e*np.sin(E)
    Ds = (M/(2*np.pi))*N_s + t_peri
    if (Ds < 0).any():
        Ds = Ds + N_s
    if (Ds > N_s).any():
        Ds = Ds - N_s
    return(Ds)
```

Listing 5. Function for converting L_s to sol number

The computational instance of calculations for 2J H_2 production is provided in Listing 6.

```
def point_loop(file):
    sg = xr.open_dataset('StupidGridFull.nc', group='flux')
    ds = xr.open_dataset(file)
    lat = ds['lat'][0]
    lon = ds['lon'][0]
    G = np.zeros(len(ds['lon']))
    for ri in range(0,len(ds['lon'])):
        ls = ds['ls'][ri]
        hr = ds['hr'][ri]
        G[ri] = sg['flux_dw_sw'][lat,lon,ls,hr]
    lss = np.unique(ds['ls'])
    Z = 2.016
    n = 2
    F = 96485.33212
    V = 1.23
    sg = 0
    sols = np.zeros(len(lss))
    for i in range(0,len(lss)):
        sols[i] = ls2sol(lss[i]*15)
    hrs = np.arange(0,25,2)
    vals = np.zeros(13)
    try:
        P = G[:, np.newaxis, np.newaxis] * ds['j2_etaPEC_H2_2bg'] * 0.01 * Z/(n*F*V)
        zz = np.zeros((len(lss),len(ds['j2-bg1']),len(ds['j2-bg2'])))
        for i in range(0,len(lss)):
            hr_int = np.where(ds['ls']==lss[i])
            inds = np.array(ds['hr'][hr_int])
            for j in range(0,len(ds['j2-bg1'])):
                for k in range(0,len(ds['j2-bg2'])):
                    y = P[:,j,k][hr_int]
                    for m in range(0,len(inds)):
                        vals[inds[m]] = y[m]
                    z = np.trapz(vals*60*60,x=hrs*1.02569)
```

```
                zz[i,j,k] = z
    z = np.zeros((len(ds['j2-bg1']),len(ds['j2-bg2'])))
    for j in range(0,len(ds['j2-bg1'])):
        for k in range(0,len(ds['j2-bg2'])):
            y = zz[:,j,k]
            z[j,k] = np.trapz(y,x=sols)
    j2h2 = np.max(z)
    j2h2i = np.unravel_index(np.argmax(z),np.shape(z), order='C')
    h2 = j2h2 * (1/688)
    bg1 = ds['j2-bg1'][j2h2i[0]]
    bg2 = ds['j2-bg2'][j2h2i[1]]
    return([[lat,lon,0],[h2,bg1,bg2]])
```

Listing 6. Function for calculating the optimal H_2 production rate

The results from the calculation of the optimal sol-averaged 3-junction PV P_{opt} and 2-junction PEC $\dot{m}_{\text{copt}}$ and their corresponding bandgap combination were again saved as `.netCDF` files with dimensions of latitude and longitude.

The resulting PV power and PEC production for H_2 is provided in Figure 8-10 with the corresponding Bandgaps distributions over the Martian grid. The distribution of bandgaps are provided in Figure 11.

Commodity	Best efficiency at averaged solar noon	Best production over a year
Power (PV, 3-junction)	Top: 1.77 eV	Top: 1.83 eV
	Middle: 1.16 eV	Middle: 1.16 eV
	Bottom: 0.72 eV	Bottom: 0. 67 eV
H_2 (PEC, 2-junction)	Top: 1.64 eV	Top: 1.77 eV
	Bottom: 0.95 eV	Bottom: 0.83 eV

Table 7. Comparison of optimal bandgaps for different optimization strategies

5.4 Missing Location Values

We were able to complete the calculations for ∼97% of the 228475 geospatial points across the Martian grid. We found that ∼6000 of these points could not be completed due to a number of issues our method of using libRadtran for Mars-based calculations. Upon inspection, we found that the missing values were generally concentrated in areas with very low elevation below the Martian datum. Further inspection confirmed that the issues in resolving the radiative transfer were caused by errors in interpolation by the solver for the gas concentrations below the datum. However, these ∼2% of missing values do not prevent us from offering a meaningful analysis.

6 TECHNOECONOMIC CALCULATIONS

6.1 Primary Power and Energy Demands

We consider four different power production and energy storage scenarios for comparison (Fig. 12): (1) Nuclear power generation with the Kilopower system; (2) Photovoltaic power generation with

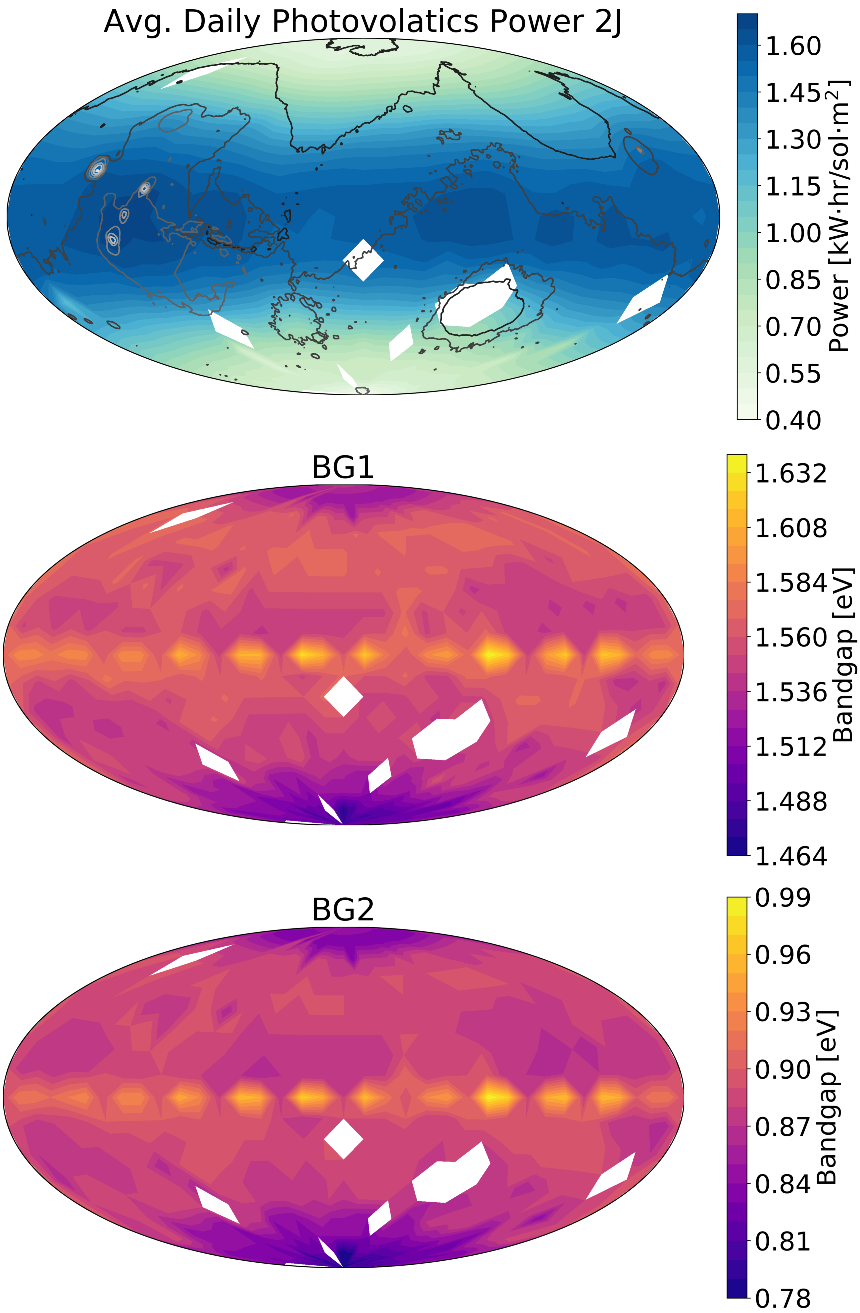

Figure 8. Two Junction Photovoltaic Power Production and Optimal Bandgaps distributed over the Martian Grid

battery energy storage; (3) Photovoltaic power generation with compressed H_2 energy storage, and (4) Photoelectrochemical H_2 generation with compressed H_2 energy storage.

In all cases, power and/or energy demand is driven by continuous power required for habitat operations, including lighting, heating/cooling, pressurization, power draw for ISRU processes, and power draw for rover travel, and by materials demand for ISRU manufacturing. We assume that ammonia, methane, and plastics are produced using H_2 as the starting material (along with N_2 and CO_2 sourced from the atmosphere), which we use to calculate power demands based on water electrolysis to produce H_2. We note that methane could be diverted for bioprocess production (dashed lines in Fig. 12), although we don't explicitly consider this scenario here since it would not change the relative mass requirements of the four systems we consider.

To compare the carry-along mass necessary for each system, we include the mass of elements unique to or uniquely sized for a given energy supply scenario. For example, we consider the mass of photovoltaic cells because the area of cells necessary to power the habitat and ISRU manufacturing will be different depending on the strategy for energy storage. However, we don't include the mass of the Sabatier reactor for methane production, since this mass will be equivalent regardless of the upstream processes producing H_2 and collecting CO_2 from the atmosphere. In this way, we can determine the mass contributions only of the uniquely necessary components for each energy supply scenario. The carry along masses are provided in Figure 13.

6.1.1 Nuclear Power

Power derived from the Kilopower nuclear reactor system is fed directly to habitat power systems and to an electrolyzer producing H_2 for ISRU manufacturing. Hence, the power draw is given by:

$$P_{\mathrm{K}} = P_{\mathrm{Hab}} + \alpha_{\mathrm{E}} \left(\dot{N}\alpha_{\mathrm{HB}} + \dot{M}\alpha_{\mathrm{S}} + \dot{B}\alpha_{\mathrm{HB}} \right) \tag{22}$$

$$P_{\mathrm{K}} = P_{\mathrm{Hab}} + \alpha_{\mathrm{E}}\Lambda \tag{23}$$

where P_{K} is the total power draw for Kilopower nuclear reactor system, P_{Hab} is the power draw for the habitat, α_{E} is the energy demand per unit of H_2 produced for the electrolyzer, $\dot{N}$ is the ammonia demand rate, $\dot{M}$ is the methane demand rate, $\dot{B}$ is the bioplastic demand rate, and α_i is the conversion factor between, e.g., the ammonia demand rate and the H_2 demand rate for the Haber-Bosch process. We also define $\Lambda = \dot{N}\alpha_{\mathrm{HB}} + \dot{M}\alpha_{\mathrm{S}} + \dot{B}\alpha_{\mathrm{HB}}$.

The carry-along mass requirements for this scenario is given by

$$M_{\mathrm{K}} = \frac{P_{\mathrm{K}}}{p_{\mathrm{K}}} + \frac{\Lambda}{p_{\mathrm{E}}} \tag{24}$$

where p_{K} is the specific power of the Kilopower reactor (6.25 W/kg) and p_{E} is the specific productivity of the electrolyzer (kg H_2/h/kg).

6.1.2 Photovoltaic power with battery energy storage (PV+B)

Power generated by photovoltaic cells can be transferred either directly to power-drawing systems (habitat systems, water electrolysis) or diverted to battery stacks for storage to enable continuous operation either at night or during low-sunlight days (due to high dust conditions). We define the fraction of power supplied directly to power systems as χ, which, for photovoltaic systems, can be thought of as the fraction of the day that solar cells produce equal or more power than what is consumed by power-drawing systems. Unless otherwise stated, we assume in our calculations $\chi = 1/3$. Hence, the total power draw for the PV+B system is given by:

$$P_{\text{PV+B}} = \chi P_{\mathrm{Hab}} + \frac{1-\chi}{\eta_{\mathrm{B}}} P_{\mathrm{Hab}} + \chi\alpha_{\mathrm{E}}\Lambda + \frac{1-\chi}{\eta_{\mathrm{B}}}\alpha_{\mathrm{E}}\Lambda \tag{25}$$

where $P_{\text{PV+B}}$ is the total power draw for the PV+B system and η_{B} is the energy efficiency of the battery storage system. More compactly,

$$P_{\text{PV+B}} = \left(\chi + \frac{1-\chi}{\eta_{\text{B}}}\right)(P_{\text{Hab}} + \alpha_{\text{E}}\Lambda) \tag{26}$$

The carry-along mass required for the PV+B scenario is given by

$$M_{\text{PV+B}} = \frac{P_{\text{PV+B}}}{p_{\text{PV}}} + \frac{(P_{\text{Hab}} + \alpha_{\text{E}}\Lambda)}{e_{\text{B}}} t_{\text{store}} + \frac{\Lambda}{p_{\text{E}}} \tag{27}$$

where p_{PV} is the specific power of photovoltaic cells, t_{store} is the desired back-up power availability time, and e_{B} is the specific energy of the battery stack (units of energy per mass).

Parameter	Value	Unit	Reference
Power and Material Demands			
P_{Hab}	40	kW	Note 6.2.1
$\dot{N}$	8.33×10^{-3}	kg h^{-1}	Note 6.2.2
$\dot{M}$	0.61	kg h^{-1}	Note 6.2.3
$\dot{B}$	0.1	kg h^{-1}	Note 6.2.4
Conversion Factors			
α_{HB}	0.196	$kgH_2\ kgNH_3^{-1}$	Note 6.2.2
α_{S}	0.554	$kgH_2\ kgCH_4^{-1}$	Note 6.2.3
α_{BP}	0.155	$kgH_2\ kgAA^{-1}$	Note 6.2.4
α_{E}	54.13	$kWh\ kgH_2^{-1}$	Note 6.2.5
α_{FC}	0.064	$kgH_2\ kWh^{-1}$	Note 6.2.5
α_{HS}	3.39	$kWh\ kgH_2^{-1}$	Note 6.2.5
Power[14] and Energy Density[15]			
p_{K}	6.25×10^{-3}	kW kg^{-1}	Note 6.1.1
η_{B}	80	%	Note 6.1.2
p_{E}	1.14×10^{-2}	$kgH_2\ h^{-1}\ kg^{-1}$	Note 6.2.5
e_{B}	0.16	kWh kg^{-1}	Note 6.1.2
p_{FC}	0.365	kW kg^{-1}	Note 6.2.5
e_{HS}	7.18×10^{-2}	$kgH_2\ kg^{-1}$	Note 6.2.5
Solar Cell Array Mess			
M_{PV}	2	kg m^{-2}	Note 6.2.6
M_{PEC}	2.4	kg m^{-2}	Note 6.2.6
Other Parameters			
χ	0.33	–	Assumed
t_{store}	24.6	h	Assumed

Table 8.

6.1.3 Photovoltaic power with H_2 energy storage

In this scenario, power generated by photovoltaic cells can either be directly fed to habitat systems or to an electrolyzer, which produces H_2 for consumption in ISRU manufacturing and for consumption by fuel cells the supply power to the habitat and other demands when direct power cannot (e.g., at night). Here, the total power demand for the system is given by

$$P_{\text{PV+E}} = \chi P_{\text{Hab}} + \alpha_{\text{E}} \dot{m}_{\text{H}_2} \tag{28}$$

where $P_{\text{PV+E}}$ is the total power draw for the PV+E system and $\dot{m}_{\text{H}_2}$ is the flow rate of H_2 necessary to support the remaining system requirements. This flow rate is written as

$$\dot{m}_{\text{H}_2} = \frac{(1-\chi)P_{\text{Hab}}\alpha_{\text{FC}} + \Lambda}{1 - \alpha_{\text{HS}}\alpha_{\text{FC}}} \tag{29}$$

where α_{FC} is the H_2 consumed per unit of energy produced by the fuel cell and α_{HS} is the energy consumed per unit of H_2 stored by the H_2 storage tanks (driven by compression of H_2).

The carry-along mass required for the PV+E scenario is given by

$$M_{\text{PV+E}} = \frac{P_{\text{PV+E}}}{p_{\text{PV}}} + \frac{\dot{m}_{\text{H}_2}}{p_{\text{E}}} + \frac{P_{\text{Hab}} + \alpha_{\text{HS}}\dot{m}_{\text{H}_2}}{p_{\text{FC}}} + \frac{(P_{\text{Hab}}\alpha_{\text{FC}} + \Lambda)t_{\text{store}}}{e_{\text{HS}}} \tag{30}$$

where p_{FC} is the specific power of the fuel cell and e_{HS} is the specific mass of the H_2 storage tanks (in units $\text{kgH}_2/\text{kg}_{\text{tank}}$).

6.1.4 Photoelectrochemical (PEC) H_2 generation with H_2 energy storage

This scenario uses an H_2 demand as opposed to a power demand to size the PEC array. The total H_2 demand rate is given by

$$\dot{m}_{\text{H}_2} = \frac{P_{\text{Hab}}\alpha_{\text{FC}} + \Lambda}{1 - \alpha_{\text{HS}}\alpha_{\text{FC}}} \tag{31}$$

The carry-along mass required for the PEC scenario is given by

$$M_{\text{PEC}} = \frac{\dot{m}_{\text{H}_2}}{m_{\text{PEC}}} + \frac{P_{\text{Hab}} + \alpha_{\text{HS}}\dot{m}_{\text{H}_2}}{p_{\text{FC}}} + \frac{(P_{\text{Hab}}\alpha_{\text{FC}} + \Lambda)t_{\text{store}}}{e_{\text{HS}}} \tag{32}$$

where m_{PEC} is the specific productivity (kgH_2/h/kg) of PEC cells. All parameters for these calculations are compiled in Table 8.

6.2 Secondary Power and Energy Demands

6.2.1 Habitat Power Demand

Continuous power demand estimates for a Martian habitat range between 4 and ~100 kW. We use 40 kW as a baseline value following the NASA Baseline Values and Assumptions Document (BVAD)[16]. This value includes ISRU power demands, including for crop growth, so we only calculated additional power demands for H_2 production for the ISRU processes considered.

6.2.2 Ammonia Demand

To calculate an upper-bound ammonia demand, we followed the optimization strategy by Do *et al.* assuming no recycling of nitrogen via urea recovery[17]. Briefly, we assumed that the metabolic demands for six crew members would be met entirely by food crops grown in hydroponic chambers. We used values from the BVAD and related literature to calculate nitrogen demand per nutrient availability for a given crop[16, 18]. The optimization function was defined to balance minimization of area necessary for crop growth with maximization of crop variability for human morale as

$$f = w_1 \sum_i A_i + w_2 \sigma(\boldsymbol{A}) \tag{33}$$

$$s.t. : \sum_i A_i r_i x_{i,j} > X_j \tag{34}$$

where f is the optimization function, A_i is the growth area for crop i, σ is the standard deviation of the vector of crop areas ($\boldsymbol{A}$), r_i is the static growth rate, $x_{i,j}$ is the nutritional content of crop i for nutrient j, and X_j is the crew member demand for nutrient j. The relative weights w_1 and w_2 are related by

$$w_2 = 1 - w_1 \tag{35}$$

and w_1 was varied between 0 and 1. Using $w_1 = 0.25$, all 5 crops we considered (soybeans, wheat, lettuce, potatoes, peanuts) were included, resulting in a total crop growth area of ∼421 m^2 and an ammonia demand of ∼205 g/sol, which we converted to 8.33 g/h for consistent units in Table 8. The nitrogen demand ranged between ∼285 g/sol and ∼194 g/sol for $0 < w_1 < 1$.

We assume ammonia is produced via the Haber-Bosch process with the characteristic reaction

$$N_2 + 3H_2 \rightarrow 2NH_3 \tag{36}$$

Hence, the H_2:NH_3 conversion factor is 0.196 $kgH_2/kgNH_3$ assuming 90% conversion of H_2.

6.2.3 Methane Demand

Resupply and crew member return to Earth from Mars will require that interplanetary transit vehicles can be refueled on Mars. We use the estimate by Kleinhenz and Paz[19] that such refueling requires 6978 $kgCH_4$ produced every 480 sols, corresponding to a CH_4 production rate of 0.61 kg/h. We assume this methane is produced via the Sabatier reaction:

$$CO_2 + 4H_2 \rightarrow CH_4 + 2H_2O \tag{37}$$

resulting in an H_2:CH_4 conversion factor of 0.554 kg $H_2/kgCH_4$ assuming 90% conversion efficiency.

6.2.4 Bioplastics and Biopharmaceutical Demand

Bioplastics and pharmaceutical demands for a Martian habitat are not well-defined in the literature. For a system where 50% of spare parts necessary for a habitat are generated via additive manufacturing based on ISRU, Owens *et al.* estimated that 9800 kg of spare parts mass would be necessary over 260 months (an extremely long duration with multiple resupplies and crew member exchanges)[20] Assuming these spares are generated from bioplastics, which are in turn produced from acetic acid at 50% yield by C_2 feedstock-utilizing microorganisms[21], this corresponds to ∼0.1 kg/h acetic acid demand. We assume acetic acid is produced by acetogens with a molar ratio of 4.2:1 (corresponding to 95% of H_2 reducing power diversion to acetic acid production, a common value for acetogens), this corresponds to an H_2:CH_3COOH ratio of 0.155 kgH_2/kg CH_3COOH assuming 90% conversion.

Pharmaceutical demand is not expected to exceed 1 g/sol, so we neglect this amount for the purposes of our calculations here.

6.2.5 Water electrolyzer, H_2 fuel cell, and H_2 storage systems

Water electrolysis and H_2 fuel cell power demands are based on commercially available, low-weight fuel cell systems designed for transportation vehicles[2]. The electrolyzer requires 54.13 kWh/kgH_2, while the fuel cell requires 0.064 kgH_2/kWh. We assume H_2 storage is accomplished with Type IV compression chambers at 350 bar, which stores H_2 at 20.77 kgH_2/m^3 with a tank mass of 289.23 kg/m^3, corresponding to a H_2 storage density of 0.0718 kgH_2/kg[22, 23]. For these systems, 3.39 kWh/kgH_2 is required to compress H_2 to 350 bar, which we account for in the total power demand[22].

6.2.6 Solar Cell Array Mass

Commercial low-weight, flexible solar cell arrays have an installed mass of 2.0 kg/m^2[3]. We are not aware of similarly commercial PEC arrays, so we assume that the installed mass is driven primarily by the absorber material as opposed to the catalyst layers or ion exchange membrane. We therefore estimate an installed mass of 2.4 kg/m^2 by assuming the absorber and housing components comprise 80% of the installed mass.

REFERENCES

[1] Bingham SJ, Lewis SR, Read PL, Forget F, Hourdin F, Talagrand O, et al. The Mars Climate Database. Tech. rep. (2003).

[2] Patel MR, Bérces A, Kerékgyárto T, Rontó G, Lammer H, Zarnecki JC. Annual solar UV exposure and biological effective dose rates on the Martian surface. *Advances in Space Research* **33** (2004) 1247–1252.

[3] Vicente-Retortillo A, Valero F, Vazquez L, Martinez GM. A model to calculate solar radiation fluxes on the Martian surface. *Journal of Space Weather and Space Climate* **5** (2015) A33.

[4] Mayer B, Kylling A. The libRadtran software package for radiative transfer calculations-description and examples of use. *Atmospheric Chemistry and Physics* **5** (2005) 1855–1877.

[5] Emde C, Buras-Schnell R, Kylling A, Mayer B, Gasteiger J, Hamann U, et al. The libRadtran software package for radiative transfer calculations (version 2.0. 1). *Geoscientific Model Development* **9** (2016) 1647–1672.

[6] Wiscombe WJ. Improved Mie scattering algorithms. *Applied optics* **19** (1980) 1505–1509.

[7] Haberle RM, Kahre MA, Hollingsworth JL, Montmessin F, Wilson RJ, Urata RA, et al. Documentation of the NASA/Ames Legacy Mars Global Climate Model: Simulations of the present seasonal water cycle. *Icarus* **333** (2019) 130–164.

[8] Mayer B, Kylling A, Emde C, Hamann U, Buras R. libRadtran user's guide. *Edition for libRadtran version* **1** (2012).

[9] Rees MH. *Physics and chemistry of the upper atmosphere* (Cambridge University Press) (1989).

[2] G-HFCS-6kW Hydrogen Fuel Cell Power Generator (Fuel Cell Store, Product Code: 1035012)

[3] MiaSolé Flex-03W Series Module with adhesive

[10] Dahlback A, Stamnes K. A new spherical model for computing the radiation field available for photolysis and heating at twilight. *Planetary and Space Science* **39** (1991) 671–683.

[11] Hanna MC, Nozik AJ. Solar conversion efficiency of photovoltaic and photoelectrolysis cells with carrier multiplication absorbers. *Journal of Applied Physics* **100** (2006) 74510.

[12] Döscher H, Geisz JF, Deutsch TG, Turner JA. Sunlight absorption in water–efficiency and design implications for photoelectrochemical devices. *Energy & Environmental Science* **7** (2014) 2951–2956.

[13] Hu S, Xiang C, Haussener S, Berger AD, Lewis NS. An analysis of the optimal band gaps of light absorbers in integrated tandem photoelectrochemical water-splitting systems. *Energy & Environmental Science* **6** (2013) 2984–2993.

[14] Hannan MA, Hoque MM, Hussain A, Yusof Y, Ker PJ. State-of-the-art and energy management system of lithium-ion batteries in electric vehicle applications: Issues and recommendations. *Ieee Access* **6** (2018) 19362–19378.

[15] Eftekhari A. Energy efficiency: a critically important but neglected factor in battery research. *Sustainable Energy & Fuels* **1** (2017) 2053–2060.

[16] Anderson MS, Ewert MK, Keener JF. Life support baseline values and assumptions document. Tech. rep. (2018).

[17] Do S, Owens A, Ho K, Schreiner S, de Weck O. An independent assessment of the technical feasibility of the Mars One mission plan–Updated analysis. *Acta Astronautica* **120** (2016) 192–228.

[18] Wheeler RM, Sagar J, Prince R, Knott W, Mackowiak C, Stutte G, et al. Crop production for advanced life support systems-observations from the Kennedy Space Center Breadboard Project. Tech. rep., NASA Ames Research Center, Mountain View, CA (2003). doi:NASA/TM-2003-211184.

[19] Kleinhenz JE, Paz A. An ISRU propellant production system for a fully fueled Mars Ascent Vehicle. *10th Symposium on Space Resource Utilization* (2017), 423.

[20] Owens A, Do S, Kurtz A, Weck Od. Benefits of additive manufacturing for human exploration of Mars. *45th International Conference on Environmental Systems* (45th International Conference on Environmental Systems) (2015).

[21] Berliner AJ, Hilzinger JM, Abel AJ, McNulty MJ, Makrygiorgos G, Averesch NJH, et al. Towards a Biomanufactory on Mars. *Frontiers in Astronomy and Space Sciences* **8** (2021) 120. doi:10.3389/fspas.2021.711550.

[22] Di Profio P, Arca S, Rossi F, Filipponi M. Comparison of hydrogen hydrates with existing hydrogen storage technologies: Energetic and economic evaluations. *International Journal of Hydrogen Energy* **34** (2009) 9173–9180.

[23] Barthélémy H, Weber M, Barbier F. Hydrogen storage: recent improvements and industrial perspectives. *International Journal of Hydrogen Energy* **42** (2017) 7254–7262.

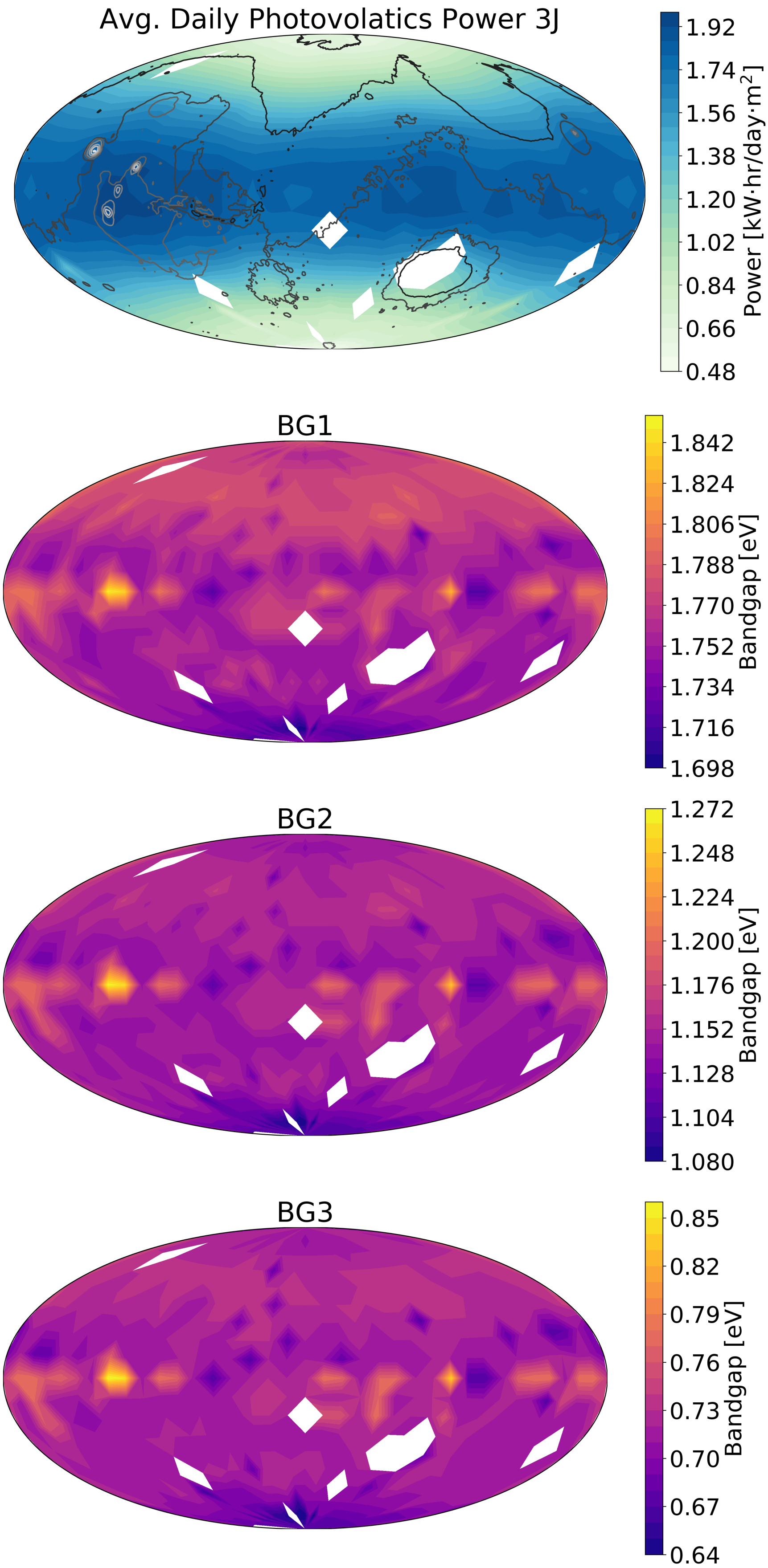

Figure 9. Three Junction Photovoltaic Power Production and Optimal Bandgaps distributed over the Martian Grid

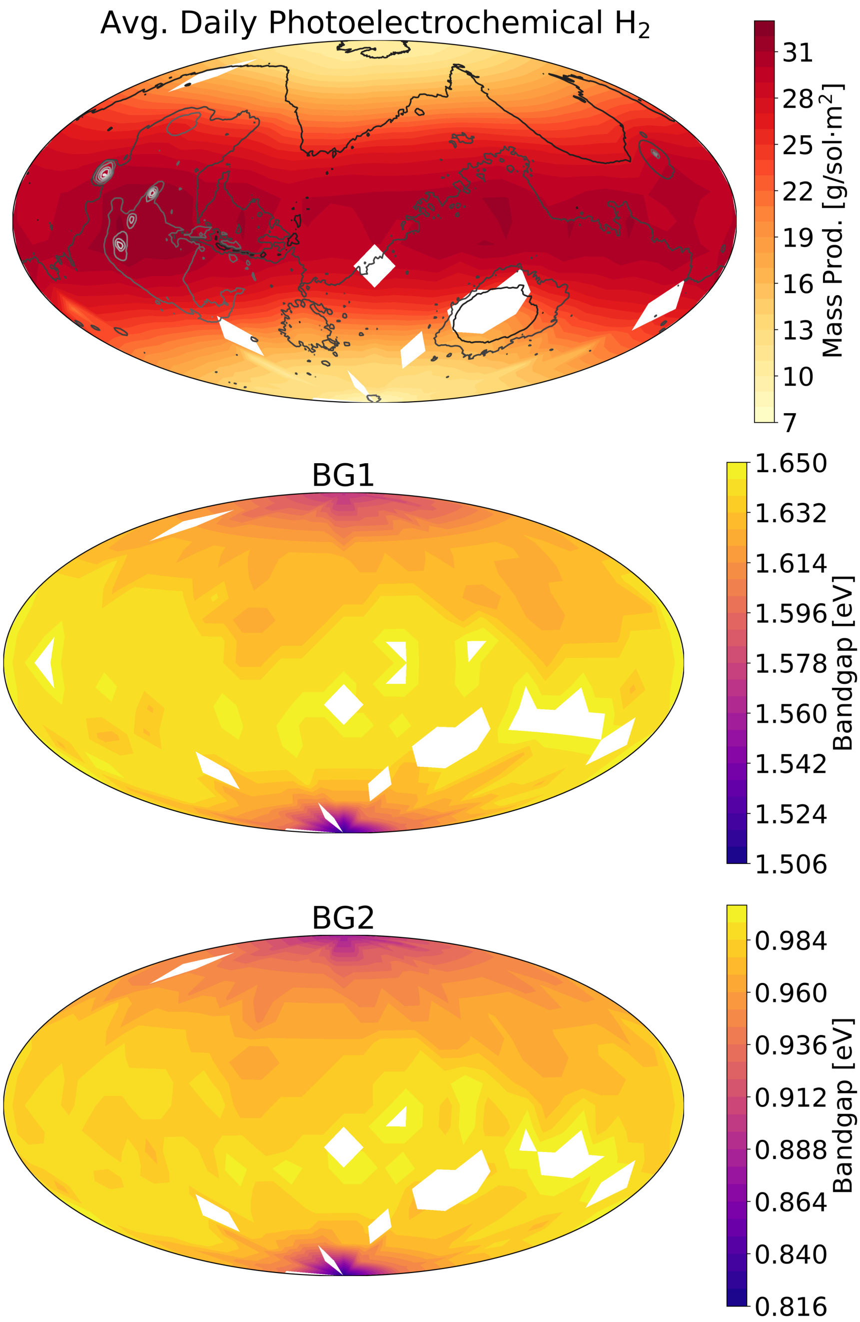

Figure 10. Two Junction Photoelectrochemical H_2 Production and Optimal Bandgaps distributed over the Martian Grid

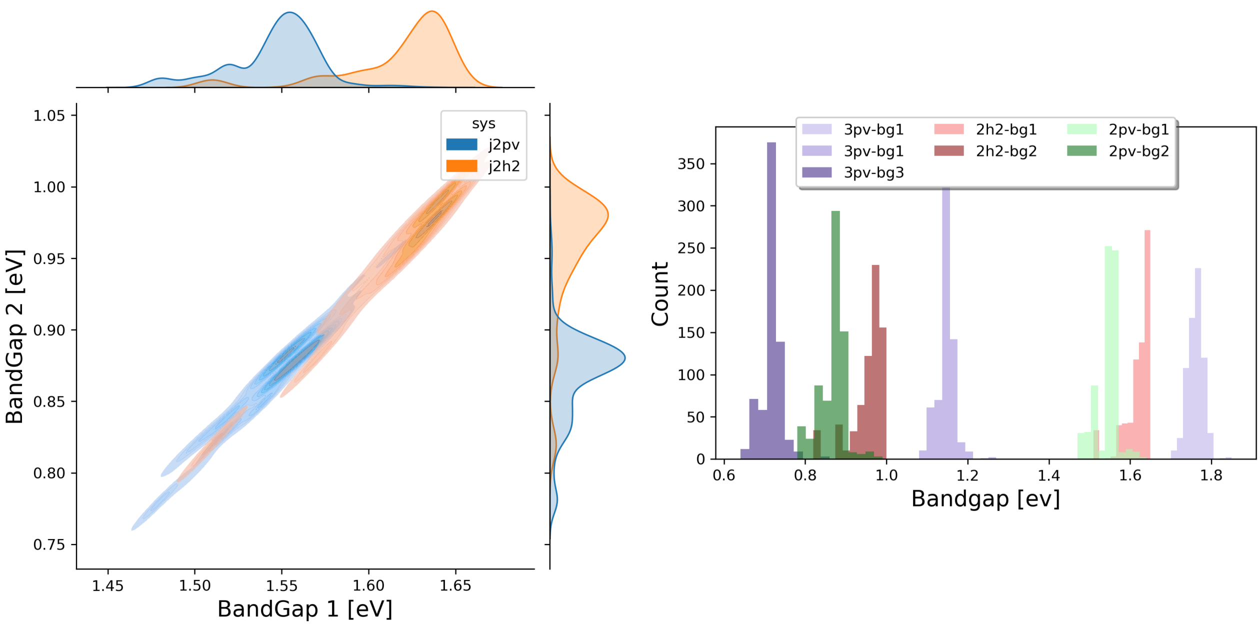

Figure 11. Optimal Bandgap Distributions.

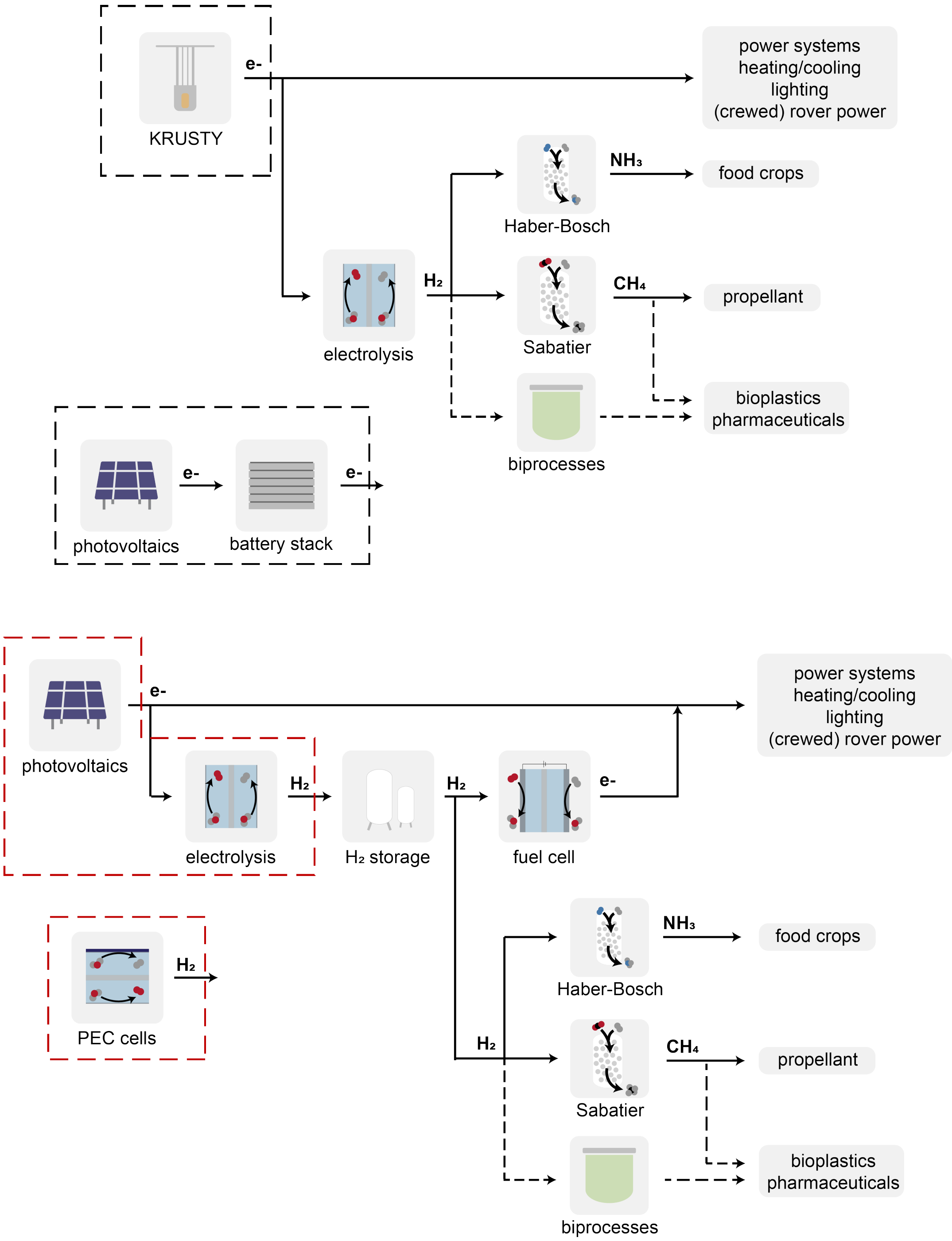

Figure 12. Power generation systems options. Habitat power systems and ammonia, propellant, and bioplastics production can be powered by nuclear power generation (KRUSTY), photovoltaics with battery storage (PV+B), photovoltaics with H2 energy storage from hydrolysis (PV+E), or photoelectrochemical H2 generation and storage (PEC).

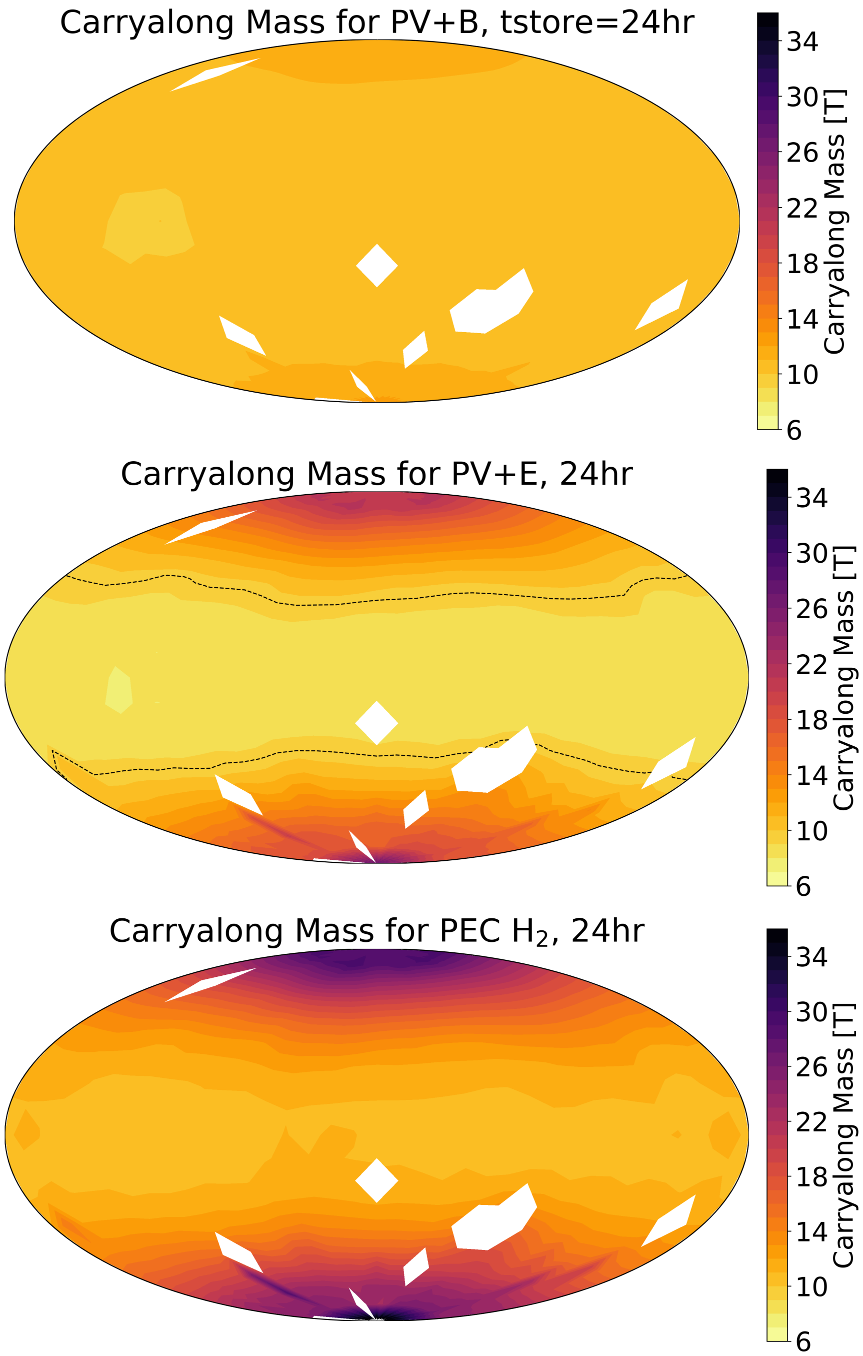

Figure 13. Carry-along mass for different power generation scenarios. Carry-along mass across the Martian surface for PV+B, PV+E, and PEC power generation systems. PV+B and PEC systems cannot reach parity with nuclear power generation in terms of carry along mass (no locations at which the projected mass of the PV+B or PEC systems is less than the projected mass of the nuclear system).